Computation of oxygen diffusion properties of the microporous layer-gas diffusion medium assembly from the combination of X-ray microtomography and focused ion beam three dimensional digital images

Mohamed Ahmed-Maloum, Thomas David, Laure Guetaz, Paul Duru, Joel Pauchet, Michel Quintard, Marc Prat

Computation of oxygen diffusion properties of the microporous layer-gas diffusion medium assembly from the combination of X-ray microtomography and focused ion beam three dimensional digital images

Mohamed Ahmed-Maloum[a], Thomas David[b], Laure Guetaz[b], Paul Duru[a], Joël Pauchet[b], Michel Quintard[a], Marc Prat[a]

[a]Institut de Mécanique des Fluides de Toulouse (IMFT), Université de Toulouse, CNRS – Toulouse, France

[b]Université Grenoble Alpes, CEA, LITEN, 38054 Grenoble, France

Abstract:

The effective diffusion properties of a gas diffusion layer (GDL) made of the assembly of a fibrous gas diffusion medium (GDM) and a microporous layer (MPL) are characterized from numerical simulations on reconstructed images obtained from combining micro X-ray computed tomography and focused ion beam-scanning electron microscopy (FIB-SEM). Using a multiscale approach, the MPL effective diffusion tensor is characterized from the FIB-SEM reconstructed 3D images considering Knudsen and Fickian diffusions. The GDM-MPL assembly effective through-plane diffusion coefficient is computed via a mixed approach combing a continuum description for the MPL and the explicit consideration of the MPL cracks and GDM fibers. The impact of cracks in the MPL is thus evaluated. A diffusive resistance model is developed to evaluate the impact of the MPL penetration into the GDM and the impact of the GDM compressibility.

Key words: PEMFC, MPL, GDL, GDM, X-ray tomography, FIB-SEM, diffusion tensor, numerical simulations

1. Introduction

Polymer Electrolyte Membrane Fuel Cells (PEMFCs) are one of the most promising technologies as power source for use in a wide range of applications in the context of the energy transition and the deployment of clean energy systems. Nevertheless, improvements in terms of performance, durability and cost effectiveness must be achieved. This can be expected from improved design of an elementary cell and its components. The properties of the various

components are therefore of paramount importance in this context. In relation with the water management, a key issue in the operation of PEMFC [1], it has been shown that inserting a microporous layer (MPL) between the gas diffusion medium (GDM) and the catalyst layer (CL) improves the performance [2-9]. As pointed out in [10], the improvement brought by the MPL is, however, not fully understood. A possible positive impact of the MPL is to prevent the liquid water forming by condensation in the GDM [11, 12] to reach the catalyst layer and to block the reaction sites. It has also been argued that the MPL might reduce the saturation in the GDM by reducing the number of liquid pathways through the GDM [13, 14, 15, 16]. The MPL might also act as a capillary barrier for the liquid water forming in the catalyst layer, which would be favorable for the membrane hydration, e.g. [17]. Inserting a MPL might also be beneficial in reducing the thermal and electrical contact resistances between the GDM and the catalyst layer [18]. Also, cracks are generally present in the MPL. However, the role of the cracks in the performance improvement due to the MPL is still unclear. Cracks might provide preferential liquid water pathways limiting the number of liquid water entry points in the GDM, which could be beneficial to the oxygen access toward the cathode catalyst layer. On the other hand, it has been reported that cracks might degrade the performance [19, 20]. In this context, characterizing the MPL, the GDM and the MPL-GDM assembly in terms of structure and properties is a natural step in order to better understand the impact of the MPL and the MPL-GDM assembly. As reviewed for instance in [21], numerous studies have been performed to characterize the properties of various GDLs with or without MPL. However, as pointed out in [22], the studies allowing to differentiate the impact of the GDM and the MPL are much scarce. A reason is that the mean pore size in the MPL is in the submicronic range (on the order of a hundred of nanometers) whereas the pore size in the GDM are much bigger (on the order of a few tens of micrometers). As exemplified in [22], analyzing the GDM-MPL assembly then imposes to combine various techniques when the characterization is sought from high-resolution 3-D imaging techniques, a powerful and increasingly used approach to characterize porous materials [23], [24]. In this work, the GDM-MPL assembly is characterized by combining focused ion beam –scanning electron microscopy (FIB-SEM) [24] and X-ray computed tomography (XCT) [23]. The MPL is characterized via FIB-SEM thanks to the high resolution achievable with this technique with voxel size of 5 nm whereas the GDM fibrous material and the cracks in the MPL are characterized via XCT with 1 μm voxel size. Using FIB-SEM combined or not with XCT to characterize the MPL or the GDM-MPL assembly is not a novelty. In [25], MPL digital images were obtained via FIB-SEM and MPL permeability and tortuosity were determined from Lattice Boltzmann Model (LBM) simulations. However,

the numerical simulations were restricted to the MPL. Furthermore, the cracks were not characterized, nor considered in the simulations. A more comprehensive characterization study of the GDM-MPL assembly combining FIB-SEM and XCT was developed by Wargo et al. [22]. However, Knudsen diffusion was not considered and only the through-plane direction was considered in the characterization of the diffusive transport. FIB-SEM imaging was also used in [26] to characterize the MPL. Only the MPL was characterized. The MPL effective diffusion coefficient was determined but only in the through-plane direction and the impact of the cracks was not considered. FIB-SEM and XCT were also combined in [27] to characterize the GDM and the MPL microstructures. The tortuosity was characterized using a random walk method. However, the cracks in the MPL were not considered and no direct numerical simulations considering the Knudsen diffusion were performed. In [28], MPL digital 3-D images were obtained using a dedicated nano-scale X-ray computed tomography technique. Only a crack-free MPL subdomain was considered. By contrast to these studies, the MPL, GDM and the GDM-MPL assembly with full consideration of the MPL cracks are considered in the present work. The effective oxygen diffusion tensor of the MPL is computed considering Knudsen and Fick diffusion. The through-plane diffusive property of the GDM-MPL assembly is characterized with a special attention devoted to the impact of MPL cracks. All the computations are performed considering dry media, i.e. in the absence of liquid water in the pores.

The paper is organized as follows. The imaging of the MPL and the GDM-MPL assembly via FIB-SEM and XCT is presented in Section 2. The numerical methodology used to compute the effective diffusion properties is presented in Section 3. Results of simulations are presented in Section 4. A discussion is proposed in Section 5. Section 6 consists of the main conclusions of the study.

2. MPL FIB-SEM and GDM-MPL XCT imaging

A Sigracet®SGL 22BB sample was selected to perform the study and analyze the MPL, the GDM and the GDM-MPL assembly.

2.1 *MPL microstructure via FIB-SEM*

3D FIB-SEM data was acquired on a Zeiss Crossbeam 550. For the MPL, a volume of 10 µm by 10 µm by 7.5 µm was imaged with pixel size of 5 nm and inter-slices distance of 5 nm too, resulting in cubic voxel of 5x5x5 nm^3. The FIB milling was done at 30kV with a current of 700 pA, and electron column was operated at 1.2 kV and 1 nA. Images from InLens and SE2

detectors were acquired simultaneously. Image processing before segmentation included slice-to-slice alignment, homogenization of contrast/brightness in all three directions, correction of curtaining effect and resampling in z direction to correct for non-homogeneous inter-slice distances during milling and imaging. These steps were done thanks to homemade python scripts based on usual image processing python libraries (e.g. numpy, scikit-image…). Segmentation was done thanks to machine learning based on random forest classifier with ilastik software [29] using the 'pixel classification' workflow. The annotation and training phase was done on a sub-volume of 192 x 196 x 400 pixels.

The 3D segmented image of the MPL microstructure obtained via FIB-SEM is shown in Figure 1a. In order to characterize the heterogeneity of the sample, the image is partitioned in adjacent cubes of size *L*. The MPL porosity is characterized by computing the void volume fraction in each cube. This operation is performed varying the cube side length between 250 nm and the image full size (7.5 µm x 10 µm x 10 µm). The obtained results are shown in Fig.1b and illustrate the heterogeneous nature of the MPL. The porosity varies from one cube to the other for all cubic block sizes considered suggesting that a representative averaging volume (REV) can be hardly identified in the considered range of sizes. However, the variance of the porosity results for each cube size decreases monotonously with increasing cube size. This is in favour of the emergence of some REV, which should not be far from the full sample size, given the observed variance decreasing rate. The MPL porosity for the entire image is 0.71, which is significantly larger than the MPL porosity of 0.42 reported in [22] for the SGL 10BC and the value of 0.5 reported in [28] for the SGL 24BC. The value of 0.71 is in very good agreement with the value of 0.69±0.03 reported in [10] for the microporosity of the same GDL, i.e. a SGL 22 BB. In accordance with [10], it is concluded here that the MPL microporosity considered in some previous studies [30-33] for Sigracet® materials was too low. In this respect, it is interesting to notice that the characterization technique used in [10] is X-ray tomographic microscopy, and not FIB-SEM. The fact that both techniques leads to comparable results is interpreted as a good signal of result consistency.

The MPL pore size distribution is characterized with the image analysis toolbox Porespy [34] using the Maximum Sphere Inscription (MSI) method. The mean pore diameter is about 150 nm, which is about half the mean pore size reported in [10] for the SGL 10BC from the chord length distribution and about twice the average pore size (90 nn) reported in [28] for the SGL 24BC but similar to the mean pore size reported in [26] for a Johnson Matthey MPL [25].

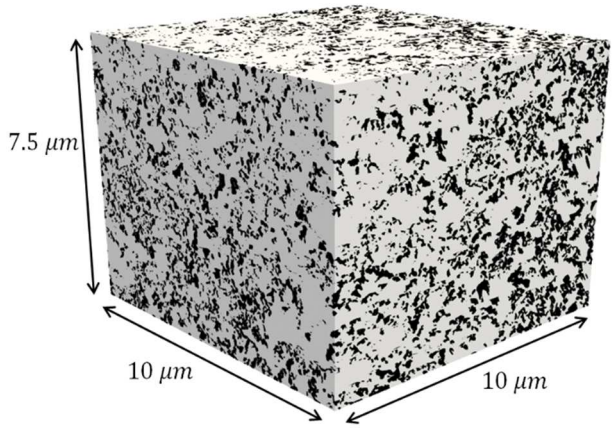

(a)

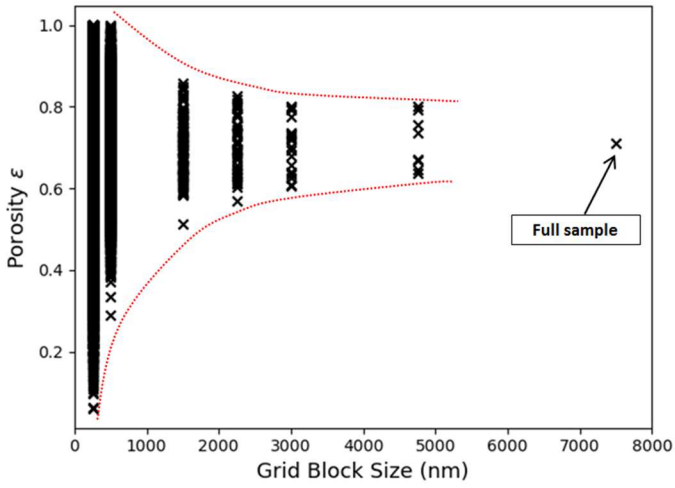

(b)

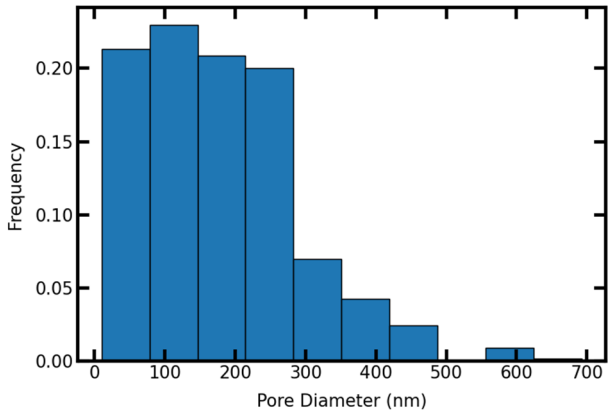

(c)

Fig.1. (a) 3D segmented FIB-SEM image of the MPL, (solid phase in black, pore space in light grey) (b) MPL porosity as a function of averaging volume (see text), (c) MPL pore size distribution.

2.2 *GDM-MPL assembly via XCT*

The body of the MPL matrix being characterized through the FIB-SEM techniques, µm-size structures (cracks, GDM) have been characterized using XCT. To this end, samples were 3D-scanned using a Phoenix Nanotom tomograph, at high spatial resolution, with an isotropic voxel size of 1 µm. Two triangular pieces of the GDM-MPL assembly were cut with a chisel and inserted in a glass capillary tube with a 2 mm inner diameter. Two pieces of GDM-MPL assembly were used in order to have a high-enough contrast during the alignment procedure of the capillary tube, source and flat panel detector, which relies on live visualizations of X-ray radiographs. Only the top part of the samples, which stood slightly above the capillary tube top end, was exposed to the X-ray beam and thus 3D scanned. Image acquisition was performed at a 50 kV voltage and 275 µA amperage. 1440 radiographies were taken with an exposure time of 1000 ms and 4 frames averaging for a total scan time of around 2 hours. Correction of ring artefacts and reconstruction was performed using Phoenix Datos|X software and tomographic slices were exported for further image processing. Avizo software was then use to denoise the tomographic slides (using a 3D non local mean filtering algorithm) and to segment them, i.e. to separate the different constitutive materials.

The resolution of the XCT image (~1 µm) does not allow to capture the sub-micronic pores in the MPL but allows to capture the GDM-MPL microstructure with an overall size adequate to characterize the GDM fibrous material, the "diffuse" MPL-GDM interface, and the crack network in the MPL. The 3D image of the GDM-MPL assembly obtained via XCT is illustrated in Fig.2. The MPL is shown in red and the GDM in green in Fig.2.

Cracks in the MPL are clearly visible in Fig.2. The crack pattern is similar to those reported in previous works, e.g. [10, 34-37]. In agreement with previous works, i.e. [35], the majority of these cracks are traversing the MPL thickness as illustrated in Figure 2e. The mean crack width in the image shown in Fig.2f is 14 µm whereas the mean in-plane distance between cracks is 196 µm. These lengths, illustrated in Fig. 2f, correspond to maximum inscribed circles in the cracks or in the regions between cracks determined using Porespy [34]. The corresponding distributions are shown in Fig.2f.

The porosity of the fibrous material, i.e. the GDM, is estimated as 0.88, which is consistent with previous works, e.g. [22], for uncompressed GDL whereas the porosity of the GDM-MPL assembly is 0.81. This value is obtained from the XCT image assigning the value 0.71 (obtained from the FIB-SEM image) to the MPL voxels in the XCT image. As shown in Fig. 2f, the pore sizes in the GDM determined using Porespy [34] are of a few tens of micrometers, which is also consistent with previous works, e.g. [22], and about 2-3 orders of magnitude

larger than in the MPL (Fig.1c).

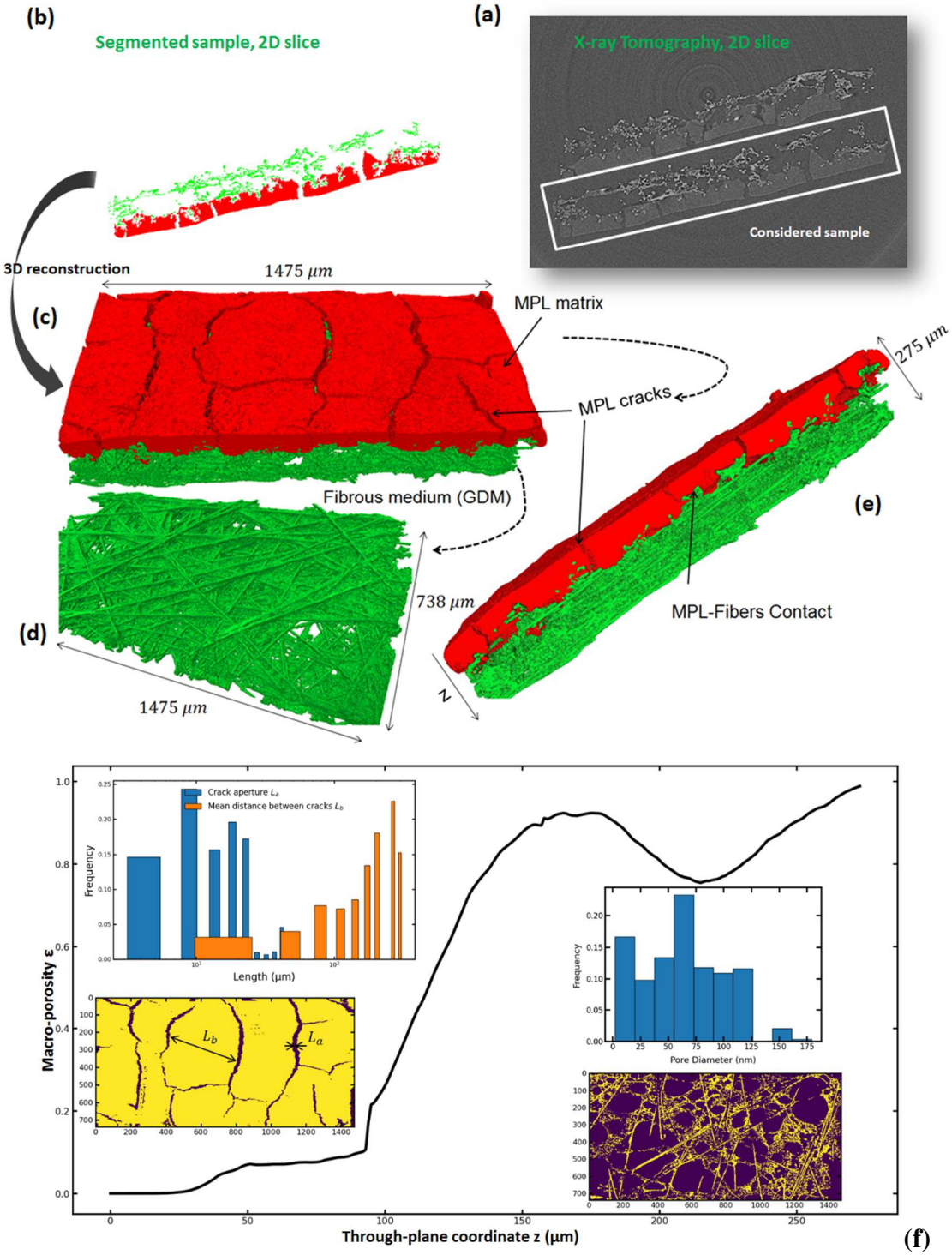

Fig.2. a) Cross-section image of the GDM-MPL assembly extracted from XCT analysis, b) segmented 2D image of the GDM – MPL assembly with the MPL in red and the GDM in green, c) 3D rendering of the GDM-MPL assembly, d) 3D rendering of the GDM, e) side view showing traversing cracks, f) GDM-MPL assembly macro-porosity variation in the through-plane direction (i.e. along the z direction shown in Fig. 2e). Insets: crack width distribution, distribution of in-plane distance between cracks, image of MPL cracks, GDM pore size

distribution and image of the GDM fibrous medium.

Fig.2f also shows the variation of the macro-porosity in the through-plane direction. The macro-porosity is the porosity determined in successive slices of thickness 1 µm (the XCT image voxel size) from the XCT images. The MPL matrix is considered as a solid phase in these images. Hence, the porosity of the MPL matrix is not included in the macro-porosity. The latter corresponds to the cracks in the MPL and the void space between the fibers in the GDM. Note that the XCT image includes a zone free of MPL (zone corresponding to z approximately smaller than 30 µm in Fig.2f.). The plateau for $50\mu m \leq z \leq 90\mu m$ in Fig.2f corresponds to the cracks in the MPL. This plateau is consistent with the fact that the cracks are weakly tortuous crossing the MPL. The zone further on the right in Fig.2f corresponds to the GDM.

3 Oxygen diffusion numerical computation

The objective is to characterize the diffusion property of the MPL-GDM assembly from numerical simulations on the 3D-images. Due to the quite large difference in the pore sizes between the GDM and the MPL a fully direct approach over the computational domain illustrated in Fig.2c is not doable (using the FIB-SEM voxel (~of size 5 nm) as elementary computational control volume, the direct computation over the domain shown in Fig.2c would correspond to a much too large computational domain with more than 10^{15} grid points !). For this reason, the solution is sought via a multiscale approach. The effective diffusion tensor is first computed for the MPL matrix, i.e. the MPL crack free region, which corresponds to the 3D image obtained via FIB-SEM (Fig. 1a). The obtained data are then used to perform the computation over the GDM-MPL assembly image obtained via XCT (Fig.2c), thus considering the MPL on the GDM surface and the fraction of the MPL that has penetrated between the GDM fibers. At the scale of the GDM-MPL assembly, the MPL is therefore considered as a continuum material containing a discrete network of cracks.

3.1 Pore scale diffusion transport governing equation

In the absence of chemical reaction and other mechanisms that could enhance the multicomponent character of the diffusion process, it is acceptable to describe the oxygen transport by diffusion at the pore scale through the Fickian diffusion equation

$$\frac{\partial c}{\partial t} = \nabla.(D(x)\nabla c) \tag{1}$$

where c is the oxygen concentration and D is the local diffusion coefficient. Given the small pore sizes in the MPL, Knudsen diffusion [38] must be considered in conjunction with Fick's diffusion. As in several previous works, e.g. [39] and references therein, our approach is based on the Bosanquet relation [40] combining the molecule-wall and molecule-molecule interactions according to the formula,

$$D(x) = \frac{1}{D_{bulk}^{-1} + D_{Kn}^{-1}} \tag{2}$$

where D_{bulk} is the bulk diffusion coefficient and D_{Kn} is the Knudsen diffusion coefficient. The latter is expressed as

$$D_{Kn} = \frac{d_p}{3}\sqrt{\frac{8RT}{\pi M}} \tag{3}$$

where R, M, T, d_p are the ideal gas constant, molar mass, temperature and pore diameter, respectively. A first hint on the significance of Knudsen diffusion can be gained from the computation of the Knudsen number,

$$Kn = \frac{\ell}{d_p} \tag{4}$$

where $\ell = \frac{RT}{\sqrt{2}\pi d_{mol}^2 N_A P}$ is the mean free path (P is the pressure, d_{mol} is the molecular diameter and N_A is the Avogadro number). As illustrated in Figure 3a, the Maximum Sphere Inscription (MSI) method is used to determine the local pore diameter d_p using Porespy [34]. The method, e.g. [41], consists in determining for each pore voxel the maximum sphere radius that can include this voxel. This leads to segment the pore space into a set of several spheres of different characteristic length (diameter).

Fig.3b shows the variation of the Knudsen number so obtained for standard PEMFC operating conditions (P ~1.5 bar, T ~ 80°C). As can be seen, the Knudsen number is lower than 1 except in a few pores in the MPL, where Kn can be on the order of 1.2. According to [42], the Bosanquet formula Eq. (2) can be used with some confidence in this range of Knudsen number, based on Molecular Dynamics simulations for one dimensional channels. Nevertheless, doubts subsist about the accuracy of the approach for complex pore structures. Addressing this problem would require heavy MD simulations, which are beyond the scope of the present work. This must be kept in mind when discussing the results. Only significant differences can be considered as non-questionable. It is important to notice that the non-negligible values of the Knudsen number in the MPL make the coefficient $D(x)$ in Eq.(1) dependent on the considered location in the pore space.

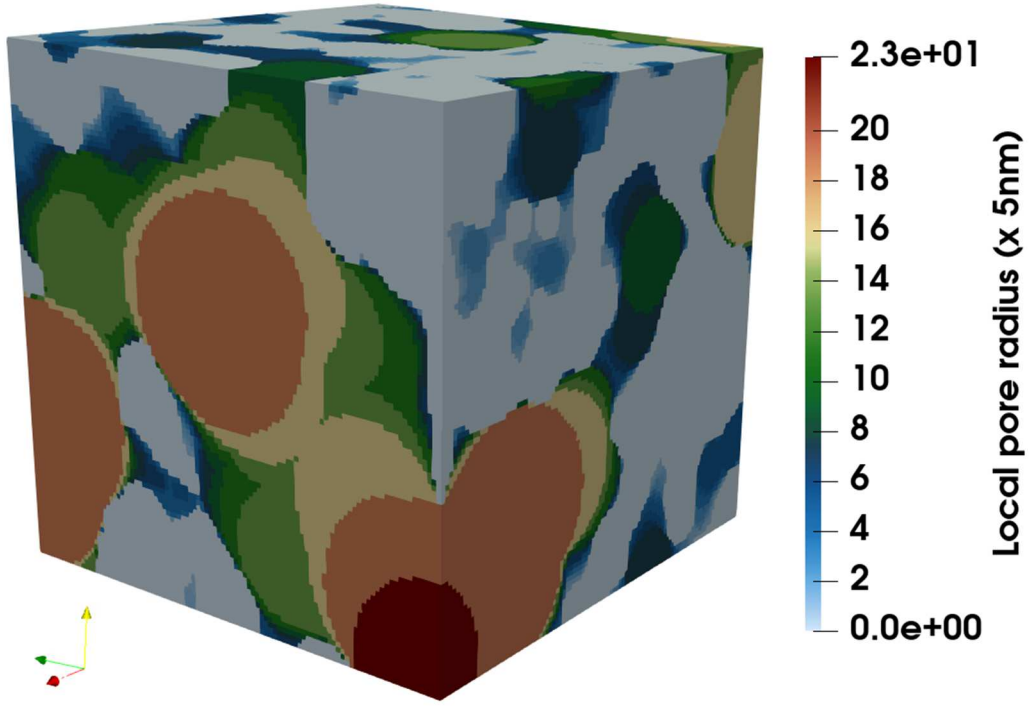

(a)

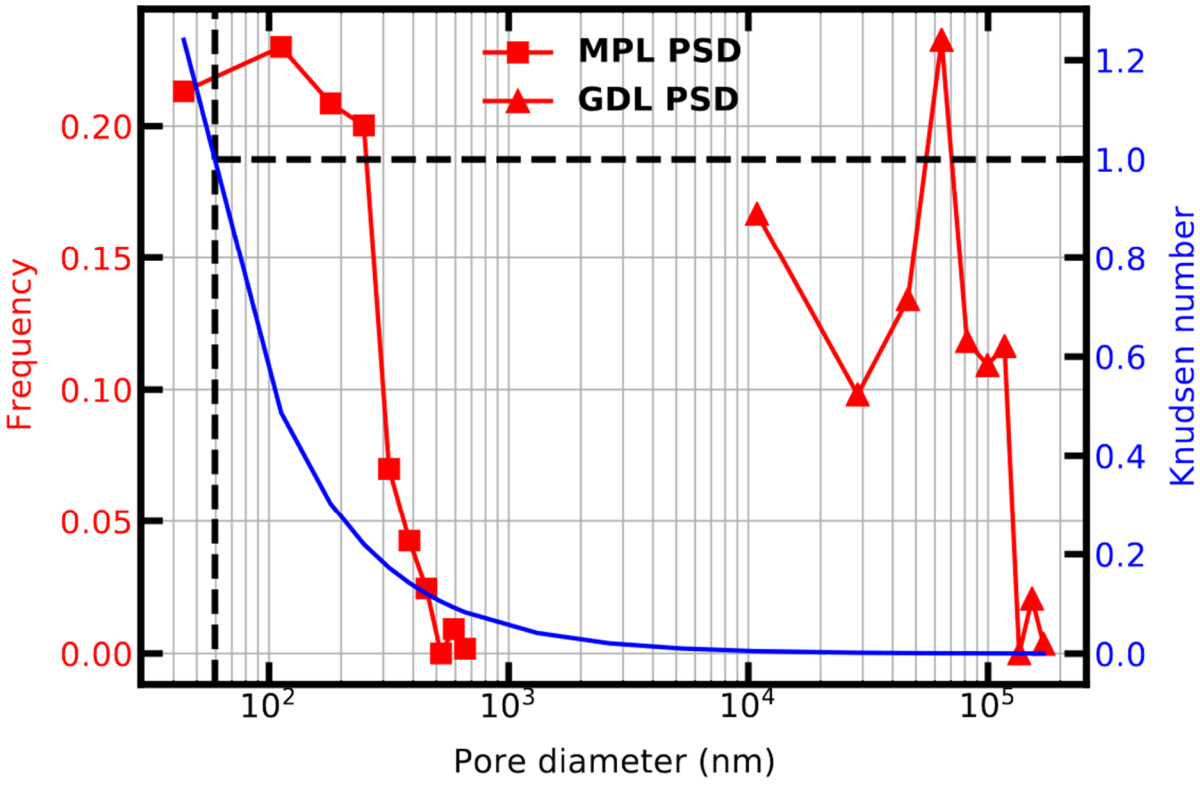

(b)

Fig. 3. (a) Local pore size radius in a MPL sub-sample from MSI method (solid phase in light grey, inscribed spheres in pore space in color), (b) Knudsen number distribution in MPL and

GDM for P = 1.5 bar and T = 353 K.

3.2 Upscaled diffusion transport governing equation in MPL matrix (outside the cracks)

According to the volume averaging method [43], the upscaled diffusion transport governing equation reads,

$$\varepsilon \frac{\partial C}{\partial t} = \nabla . (\varepsilon \mathbf{D}_{eff} . \nabla C) \quad (5)$$

Where ε is the MPL local porosity and $\mathbf{D}_{eff}$ is the effective diffusion tensor; C can be interpreted as the intrinsic average concentration over the averaging volume, see [43] for more details. Within the framework of the volume averaging method, the derivation of Eq.(5) is associated with the use of a small parameter, which is the ratio of the averaging volume size to the size of the porous medium domain (the MPL here) or equivalently with the existence of a representative elementary volume (REV) whose size is small compared to the porous medium size. In this respect, based on the results on the porosity shown in Fig.1b, the validity of Eq.(5) can be questioned since no clear REV can be inferred from these results. This is a common situation encountered when dealing with heterogeneous materials [44, 45]. Following these approaches, resolution of diffusion problems at the MPL scale is carried out by a grid-block technique, which can be described as follows: Eq. (5) is resolved over a coarse numerical grid with effective diffusion tensors calculated for every grid-block based on a finer description of the structure. Because of the lack of true REV size, one can play with the coarse grid-block size to control the accuracy of the simulation. There are many advantages to this method since one does not try to homogenize the entire MPL domain. Sub-grid-block size heterogeneity effects are incorporated in every gridblock effective tensor, while coarse-scale heterogeneity effects are kept, thus, for instance, allowing to reproduce some abnormal (non-Fickian) diffusion effects induced by these heterogeneities. Incidentally, but this is very important on a practical basis, fine calculations are only carried out on the subgrid-blocks, thus limiting the need for huge computational resources. This grid-block approach can be reproduced sequentially, if needed because of computational requirements. In our case, as for the porosity characterization (Section 2), the grid-block step consists in partitioning the MPL matrix digital image in adjacent cubic blocks of equal size L. In the next section, we explain how the effective diffusion tensor is computed for a given cubic block.

3.3 Effective diffusion tensor computation over a block.

A somewhat commonly used approach to determine an effective property in one direction (often the through-plane direction in PEMFC component characterization) is to impose

Dirichlet conditions, i.e. uniform concentrations over the inlet and outlet computational domain limiting surfaces perpendicular to the considered direction and spatially periodic boundary conditions in the lateral directions, e.g. [22, 26].

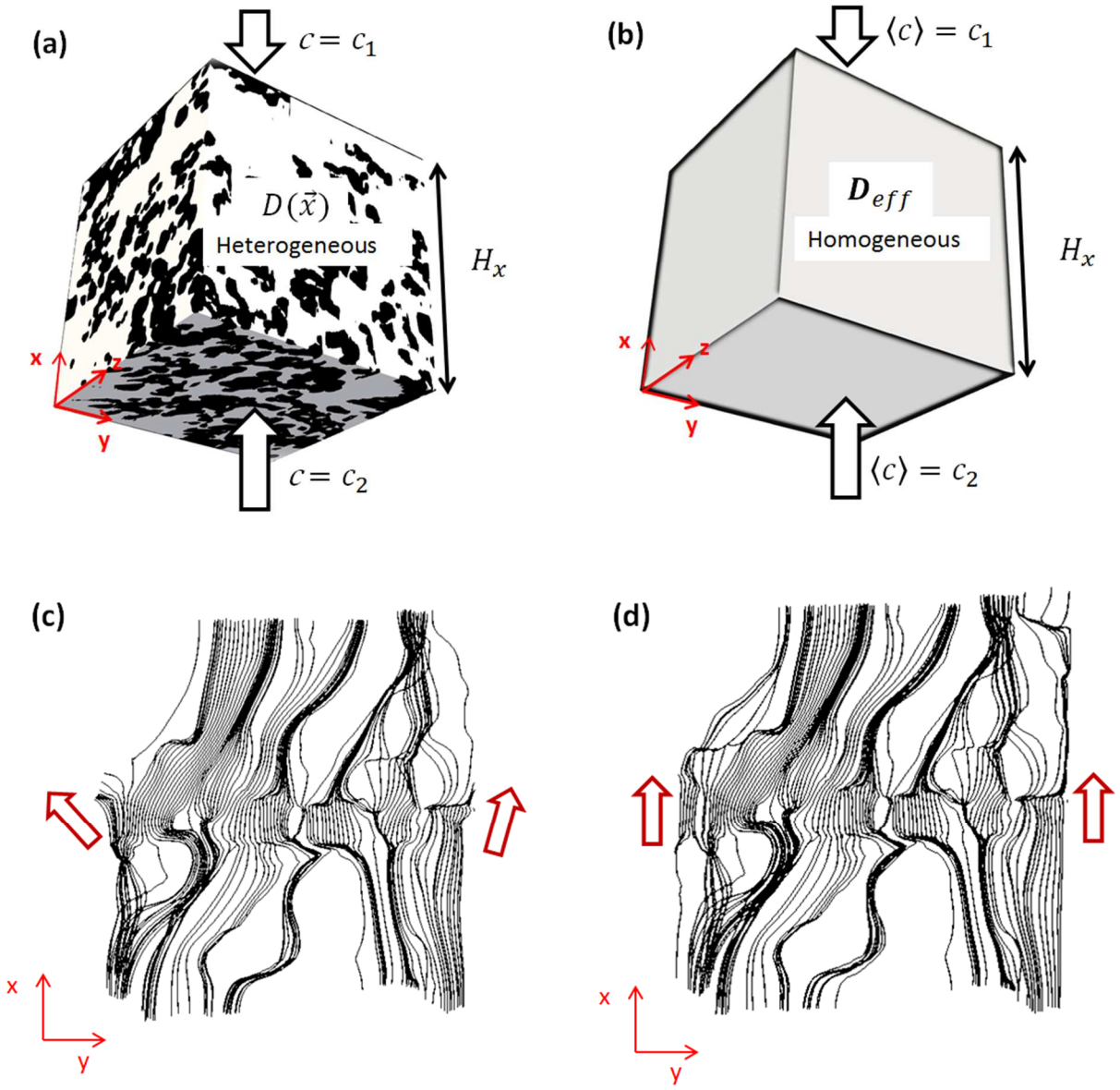

Fig.4. a) Sketch of direct numerical simulations with inlet-outlet concentration difference applied in the x-direction. b) fictitious continuum medium equivalent block, (c) and (d) diffusive flux field in a simulation using Bamberger boundary condition (c) or zero-flux boundary condition (d).

However, the MPL 3D image (Fig. 1a) or a sub-block extracted from the image are not spatially periodic and do not necessarily correspond to a spherical effective diffusion tensor. The image (or the sub-block) can be rendered spatially periodic [46] but this significantly increases the size of the image and also alter the anisotropy properties. For this reason, following [46],

spatially periodic boundary conditions are not used in what follows.

The method for estimating the effective diffusion tensor for a given grid-block is based on the following steps:

1. Perform small-scale simulation on the grid-block with given boundary conditions,
2. Perform macro-scale simulations on the same geometry, with the same boundary conditions, but this case with a homogeneous diffusion tensor. The effective diffusion tensor will be estimated in order to reproduce the average fluxes through the block as calculated in step 1.

The procedure is detailed below. Dirichlet conditions are used in one direction (as sketched in Fig. 4 with $c = c_1$ at the outlet and $c = c_2$ at the inlet) whereas two types of lateral conditions are considered: i) zero-flux conditions, ii) Bamberger conditions [47]. As explained in [46], the Bamberger condition consists in imposing a constant concentration gradient along the lateral walls, i.e. a linear variation between c_2 and c_1 along the lateral walls. This condition imposes less constraint on the computed concentration field, and therefore less biases on the computed effective property. This is illustrated in Figs. 4c and 4d showing two slices of diffusion flux isolines from two simulations, one with zero-flux boundary condition and the other with Bamberger boundary condition. Differences are clearly visible near the lateral boundaries. The diffusion flux can be non-aligned with the lateral boundaries in the case of the Bamberger condition whereas the alignment is forced with the zero-flux condition. Both boundary conditions have been tested. Tests show that both boundary conditions lead to quite close results in our case in terms of effective diffusion tensors. The conclusion is that the effective diffusion tensor can be computed considering indifferently both lateral conditions, at least in the case of the MPL considered in the present work.

The steady-state version of Eq.(1) together with the boundary conditions discussed previously is solved using the LaplacianFoam solver of the open source CFD software OPENFOAM. Note that the fact that oxygen diffusion does not occur in the solid phase is taken into account via a penalization technique consisting in imposing a very low value of the diffusion coefficient in the solid phase (~10^{-9} m^2/s, which is 10^4 smaller that the diffusion coefficient in the pores). Once the pore scale concentration field c is obtained, the average diffusive flux over the computational domain is computed as

$$\langle \boldsymbol{j} \rangle = \frac{1}{V} \int_{V_f} (-D(\boldsymbol{x}) \nabla c)\, dV \tag{6}$$

where V is the volume of the computational domain and V_f is the volume occupied by the pore space in V.

Then, the effective diffusion tensor must be determined according to Step 2 described above. This step requires that the effective diffusion tensor is estimated so as to reproduce the micro-scale average fluxes. In principle, one should solve Eq. (5) and use some optimization method to estimate $\mathbf{D}_{eff}$. However, approximate methods are available to avoid such an optimization method. They are based on approximate solutions of diffusion over the block in the case of a homogenoeus effective diffusion tensor. Let us start with the Bamberger conditions. There is a simple analytical solution that corresponds to homogeneous diffusion in a slab of infinite lateral extent. The macro-scale concentration gradient, ∇C, is uniform, as well as the macro-scale flux, *J*. The components of the effective diffusion tensor are then determined by expressing that the average flux given by Eq. (6) must be equal to the macroscopic diffusion flux, namely

$$\boldsymbol{J} = -\varepsilon \mathbf{D}_{eff}.\nabla C = \langle \boldsymbol{j} \rangle \tag{7}$$

For the configuration illustrated in Fig.4, the macroscopic gradient ∇C corresponds to $\nabla C = \frac{c_1 - c_2}{H_x}\,\boldsymbol{e}_x$, where $\boldsymbol{e}_x$ is the unit vector in the direction of *x* and H_x is the dimension of the computational domain in the *x* direction. From Eq.(7), this leads to the following relationships

$$D_{effxx} = -\frac{H_x}{\varepsilon(c_1 - c_2)}\langle j_x \rangle \tag{8}$$

$$D_{effyx} = -\frac{H_x}{\varepsilon(c_1 - c_2)}\langle j_y \rangle \tag{9}$$

$$D_{effzx} = -\frac{H_x}{\varepsilon(c_1 - c_2)}\langle j_z \rangle \tag{10}$$

The same procedure is applied in the *y* and *z* directions, which allows computing all the components of tensor $\mathbf{D}_{eff}$,

$$\begin{pmatrix} D_{effxx} & D_{effxy} & D_{effxz} \\ D_{effyx} & D_{effyy} & D_{effxz} \\ D_{effzx} & D_{effzy} & D_{effzz} \end{pmatrix}_{L_1} = -\frac{1}{\varepsilon_{L_1}(c_1 - c_2)} \begin{pmatrix} H_x\langle j_x \rangle^1 & H_y\langle j_x \rangle^2 & H_z\langle j_x \rangle^3 \\ H_x\langle j_y \rangle^1 & H_y\langle j_y \rangle^2 & H_z\langle j_y \rangle^3 \\ H_x\langle j_z \rangle^1 & H_y\langle j_z \rangle^2 & H_z\langle j_z \rangle^3 \end{pmatrix} \tag{11}$$

where indices 1, 2 and 3 correspond to the application of the inlet-outlet concentration difference $(c_1 - c_2)$ in the *x*, *y* and *z* directions, respectively. It can be noticed that here $H_x = H_y = H_z = L_1$.

There is no such an analytical solution for the computations with the zero flux lateral conditions. However, the concentration and flux fields far from the lateral boundaries are close to the Bamberger solution. Therefore, one will use the same estimation procedure as described by Eqs. (11). It must be noticed that these estimations do not impose that the effective tensor is symmetric. This is not an inconvenience, as long as the effective tensor is definite positive (see discussion in [46]).

3.4 Sequential methodology

Given the MPL image overall size (5.6 billion voxels), it is not numerically efficient to apply the procedure presented in Section 3.3 on the whole image owing to the long computational times and memory size requirements. As mentioned before, a sequential approach is adopted. This avoids very long computation times and, also, allows analyzing the distribution of effective coefficients at intermediate Darcy-scales. This is useful to discuss the existence of a REV (Representative Elementary Volume), analyze spatial heterogeneities, etc. In this work a two scale sequential procedure is developed. As displayed in Fig. 5, the whole image is partitioned into blocks of a chosen size L_1. The effective tensor $\mathbf{D}_{eff-L_1}$ is computed for each block of size L_1 according to the procedure described in Section 3.3 (Eqs. (6-11)). The diffusion problem at the scale L_2 of the whole image is then formulated as

$$\nabla.\left(\varepsilon_{L_1}(\boldsymbol{x})\mathbf{D}_{eff-L_1}(\boldsymbol{x}).\nabla C\right)=0. \tag{12}$$

with appropriate boundary conditions. In this approach, the effective diffusion properties determined for one block and is porosity are assigned to each point in the considered block. Then the procedure to determine the effective diffusion tensor at scale L_2 is similar to the one described in Section 3.3. Eq. (12) is solved numerically using the same boundary conditions as presented in section 3.3 considering successively the directions *x*, *y* and *z* to apply the inlet-outlet concentration difference (c_1-c_2) and the effective tensor components for the whole image (scale L_2) are determined using relationships similar to Eq.(11), namely

$$\begin{pmatrix} D_{effxx} & D_{effxy} & D_{effxz} \\ D_{effyx} & D_{effyy} & D_{effxz} \\ D_{effzx} & D_{effzy} & D_{effzz} \end{pmatrix}_{L_2} = -\frac{1}{\langle\varepsilon\rangle_{L_2}(c_1-c_2)} \begin{pmatrix} H_x\langle j_x\rangle^1 & H_y\langle j_x\rangle^2 & H_z\langle j_x\rangle^3 \\ H_x\langle j_y\rangle^1 & H_y\langle j_y\rangle^2 & H_z\langle j_y\rangle^3 \\ H_x\langle j_z\rangle^1 & H_y\langle j_z\rangle^2 & H_z\langle j_z\rangle^3 \end{pmatrix} \tag{13}$$

where H_x = 10 µm, H_y =10 µm, H_z=7.5 µm (Fig. 1a) and

$$\langle \boldsymbol{j}\rangle = \frac{1}{V}\int_V \left(-\varepsilon_{L_1}(\boldsymbol{x})\mathbf{D}_{eff-L_1}(\boldsymbol{x}).\nabla C\right)dV \tag{14}$$

As for the first step (Section 3.3), Eq. (12) is solved using the LaplacienFoam solver in OpenFOAM. A structured hexahedral mesh is used proportional to the voxel matrix. A subdivision factor allows refining or coarsening the mesh, depending of the size of the blocks. Computations are performed using Olympe super-calculator from the regional computational center "Calmip". The typical CPU time is about 400h to obtain the final effective diffusion tensor at scale L_2.

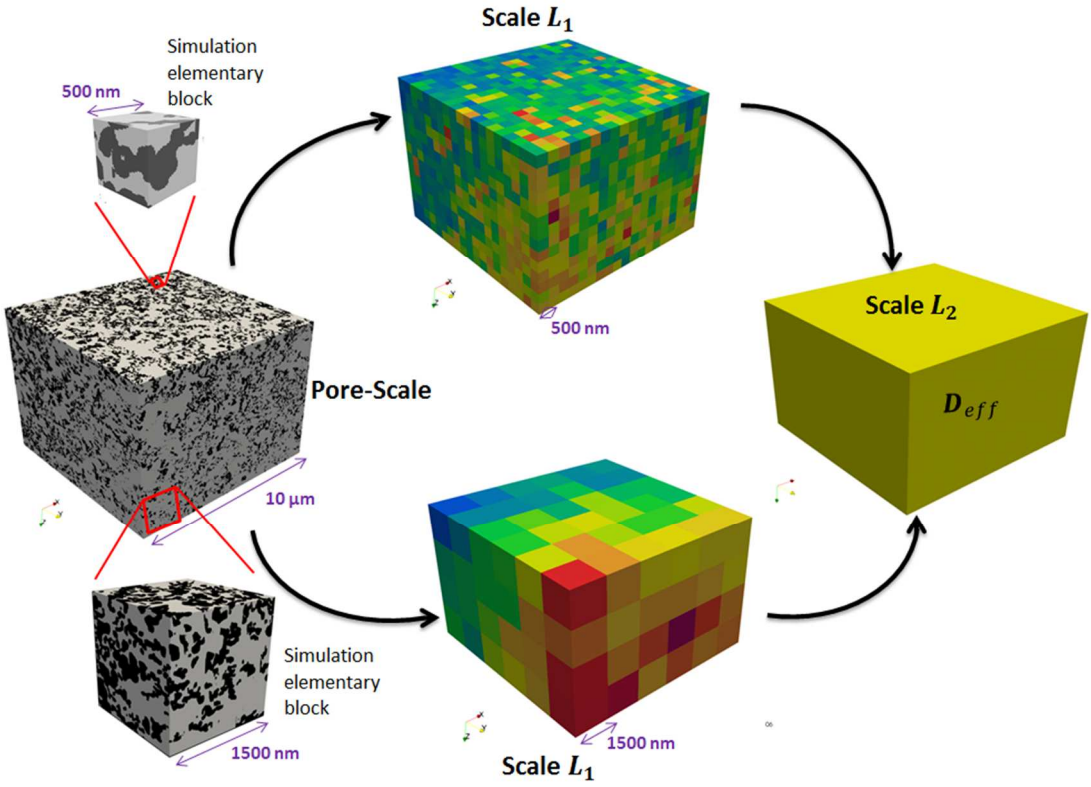

Fig.5. Two-step sequential approach for the computation of MPL effective diffusion tensor; (1) pore-scale, (2) continuum scale L_1 for two grid block size 500 nm (top) and 1500 nm (bottom) (3) continuum scale L_2

4 Results

The multiscale modeling approach imposes to calculate first the MPL properties (outside the cracks) in order to use them in the computation of the MPL-GDM assembly. Therefore, the results are presented in two parts. The MPL diffusion properties are presented first and the impact of anisotropy and Knudsen diffusion are evaluated. Then, the diffusion properties of the GDL with and without MPL are presented. Finally, the results for the GDL-MPL assembly are presented and the impact of MPL penetration into the GDL and MPL cracks are investigated.

4.1 MPL diffusion properties

In this section, the methodology described in Sec. 3 is used.

4.1.1 MPL effective diffusion tensor at block scale L_1

As illustrated in Fig. 5, the MPL effective diffusion tensor is calculated for two block sizes, namely 500 µm and 1500 µm. The distribution of the effective diffusivity components for both

block sizes is shown in Fig.6 with or without consideration of Knudsen diffusion.

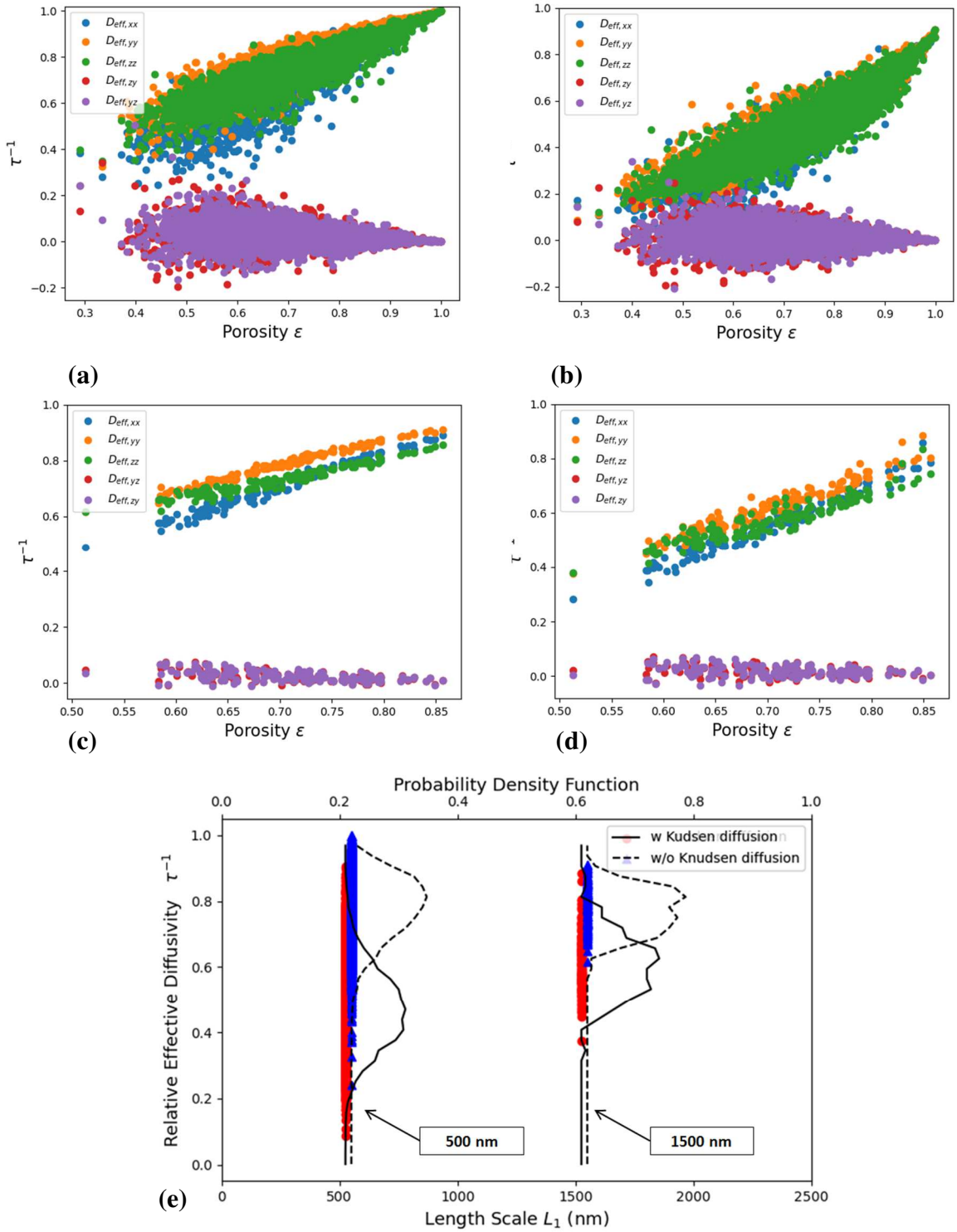

Fig.6. Distribution of the components of MPL effective diffusion tensor, (a) with block size L_1 = 500 nm and without Knudsen diffusion, (b) with block size L_1 = 500 nm and with Knudsen diffusion, (c) with block size L_1 =1500nm and without Knudsen diffusion, (d) with block size L_1 =1500nm and with Knudsen diffusion. (e) Probability density function of the relative diffusivity tensor component $D_{effxx-L_1}$, for both block sizes, with and without considering

Knudsen diffusion

It can be first noticed that the porosity varies significantly from one block to the other. The diagonal components globally increase with the porosity but the spreading of the results for a given intermediate porosity is significant when the Knudsen effect is not considered. This is another illustration of the lack of REV at this scale. The effective diffusivity tensor non-diagonal components are quite small compared to the diagonal components (less than 10% for the larger block size). The values of the tensor diagonal components are slightly different for the considered block sizes, indicating some anisotropy effects. Interestingly, the relatively small value of the off-diagonal components suggests that the principal axis are aligned with the coordinate axis. The spreading of the results is a bit less for the largest block size but remains noticeable.

As can be seen from Fig. 6 , the impact of Knudsen diffusion is significant. One notice that the spreading of the results for a given porosity is much less. Also, the off-diagonal components are quite negligible compared to the diagonal components.

Fig. 6e gives a more detailed view of the first component distribution of the effective diffusivity tensor, i.e. $D_{effxx-L_1}$, for both block sizes. This plot better illustrates the impact of Knudsen diffusion with a mean value with Knudsen diffusion that is about half the value obtained when only Fick diffusion is considered. Also, it can be seen that there is almost no overlap between both distributions for the largest block size considered. This figure also illustrates the impact of the block size on the spreading of the distribution. The larger the block size, the smaller is the spreading.

In this paragraph, the computed relative diffusion coefficient at this scale, i.e. $\frac{D_{effxx-L_1}}{D_{bulk}}$ is compared with the experimental results reported in [27] considering the same pressure (P = 201 kPa) and temperature (T = 22°C) as in [27].

As explained in [27], the experimental results were also used to extract the relative diffusion coefficient when the Knudsen diffusion is not considered. As can be seen from Fig.7, our simulation results are in a quite good agreement with the experimental results of Inoue and al. [27] for both cases, with and without consideration of the Knudsen diffusion. It can be noticed that the MPLs considered in [27] are from Gore™ and not from SGL. Nevertheless, the results are quite comparable in Fig.7. In the absence of Knudsen diffusion, the relative diffusion coefficient is classically expressed in terms of tortuosity, i.e. $\frac{D_{effxx-L_1}}{D_{bulk}} = \frac{1}{\tau}$. In the fuel cells literature, the tortuosity τ is often estimated using Bruggeman's relationship, $\tau = \varepsilon^{-0.5}$ [48], noting that the exponent value 0.5 applies for a medium made of spherical particles [48]. In

line with [48], it can be seen that Bruggeman relationship with the exponent -0.5 overestimates the relative effective diffusion coefficient.

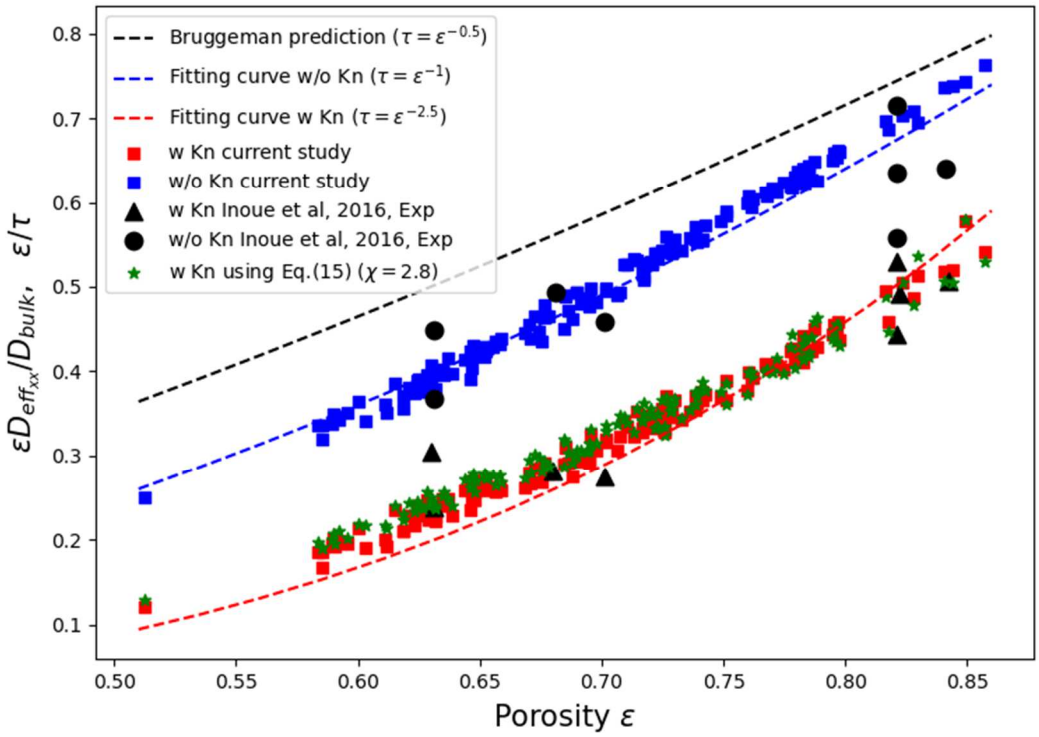

Fig.7. Comparison of the evolution of $\frac{\varepsilon D_{effxx-L_1}}{D_{bulk}}$, i.e. $\frac{\varepsilon}{\tau}$, as a function of porosity with experiment of [27] at 201 kPa of pressure and a temperature of 22°C and the analytical model of Bruggeman.

Nevertheless, it can be seen from Fig.7 that the exponent can be adjusted so as to represent reasonably well the data. When the Knudsen diffusion is considered, the exponent actually depends on the considered pressure, temperature and gas. It can be also noticed that our simulation results with Knudsen diffusion are in quite good agreement with those of Guo et al. [49] obtained from a lattice-Boltzmann model on a numerically reconstructed MPL microstructure. The following relationship is used in [49] to relate the through plane effective diffusion coefficients with or without consideration of Knudsen diffusion,

$$\frac{D_{effxx-Kn}}{D_{effxx-Fick}} = \frac{1}{1+\chi\langle Kn\rangle} \tag{15}$$

where χ is a numerical factor and $\langle Kn\rangle$ is the average Knudsen number defined as the ratio of the gas mean free path to the average pore diameter in the considered block. Adjusting parameter χ ($\chi = 2.8$) leads to the data shown with green stars in Fig.7, in quite good

agreement with the pore scale computation data obtained from the direct simulations with consideration of the Knudsen diffusion. In agreement with [49], Eq.(15) provides an effective analytical model to estimate simply the impact of Knudsen diffusion on the gas effective diffusion coefficient. It can be noted however that the adjusted value of the numerical factor χ is greater than the value reported in [49] ($\chi = 0.9$). This is indication that the value of this coefficient depends on the considered nanoporous materials since the MPL microstructure studied in [49] is not obtained from FIB-SEM but via a numerical generation procedure.

4.1.2 MPL effective diffusion tensor at scale L_2

Table 1 summarizes the result obtained at the scale of the whole MPL FIB-SEM image (L_2 scale) for both block sizes. Some slight differences can be observed between the results for both block sizes but the results are quite close, indicating a quite weak dependence of the results with the block size at this scale.

Consistently with the results at scale L_1, the off-diagonal terms can be considered as negligible. A slight anisotropy is still present. However, based on the results shown in Table 1, the hypothesis of isotropy commonly considered in the literature is quite reasonable. As for the intermediate scale L_1, the impact of Knudsen diffusion is significant with a reduction of the diagonal component by a factor 0.6 compared to the computation not considering the Knudsen diffusion.

Table 1: MPL effective diffusion tensor relative components $\left(\frac{1}{\tau}\right)$ for both block sizes

	L_1 (nm)	$\frac{D_{effxx-L_2}}{D_{bulk}}$	$\frac{D_{effxy-L_2}}{D_{bulk}}$	$\frac{D_{effxz-L_2}}{D_{bulk}}$	$\frac{D_{effyx-L_2}}{D_{bulk}}$	$\frac{D_{effyy-L_2}}{D_{bulk}}$	$\frac{D_{effyz-L_2}}{D_{bulk}}$	$\frac{D_{effzx-L_2}}{D_{bulk}}$	$\frac{D_{effzy-L_2}}{D_{bulk}}$	$\frac{D_{effzz-L_2}}{D_{bulk}}$
With Knudsen diffusion	500	0.45	-0.01	0.01	-0.01	0.49	0.011	0.01	0.012	0.46
With Knudsen diffusion	1500	0.43	-0.012	0.012	-0.012	0.48	0.013	0.012	0.013	0.44
Without Knudsen diffusion	500	0.73	-0.011	0.014	-0.011	0.8	0.021	0.014	0.022	0.75
Without Knudsen diffusion	1500	0.72	-0.012	0.016	-0.012	0.79	0.023	0.016	0.024	0.74

4.2 MPL-GDM assembly

A rendering of the GDM-MPL assembly 3D image obtained via XCT is shown in Fig.8. In

order to determine the porosities and thicknesses of the assembly components, various limiting surfaces were defined as sketched in Fig.8.

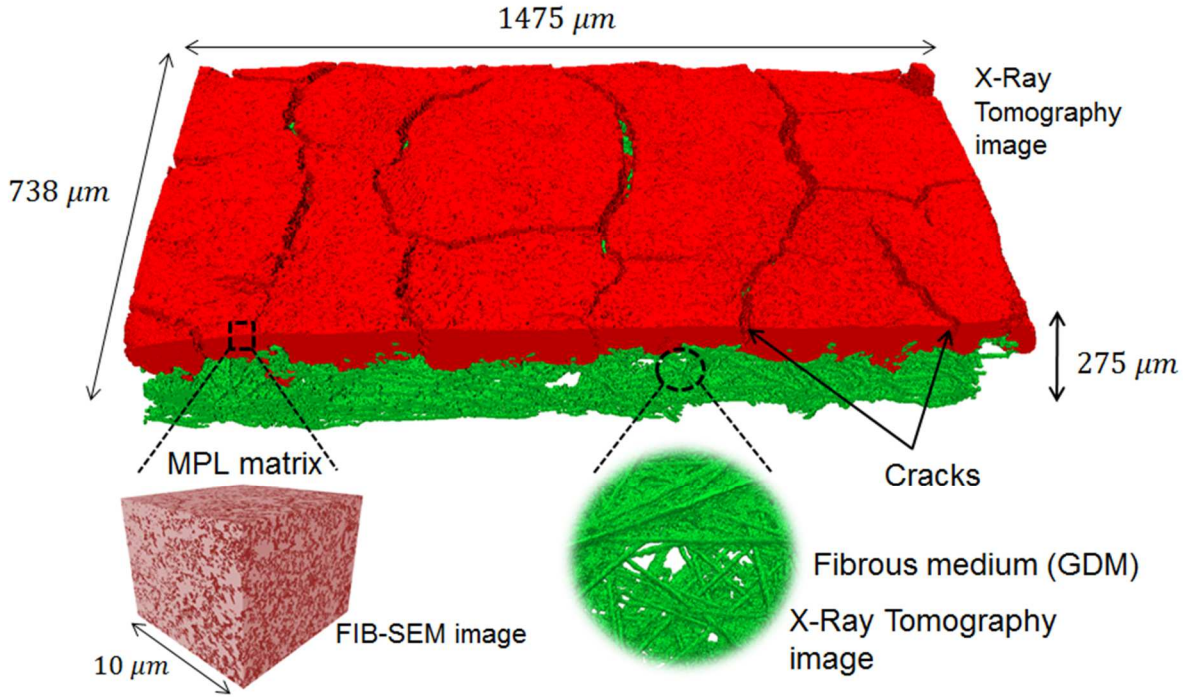

(a)

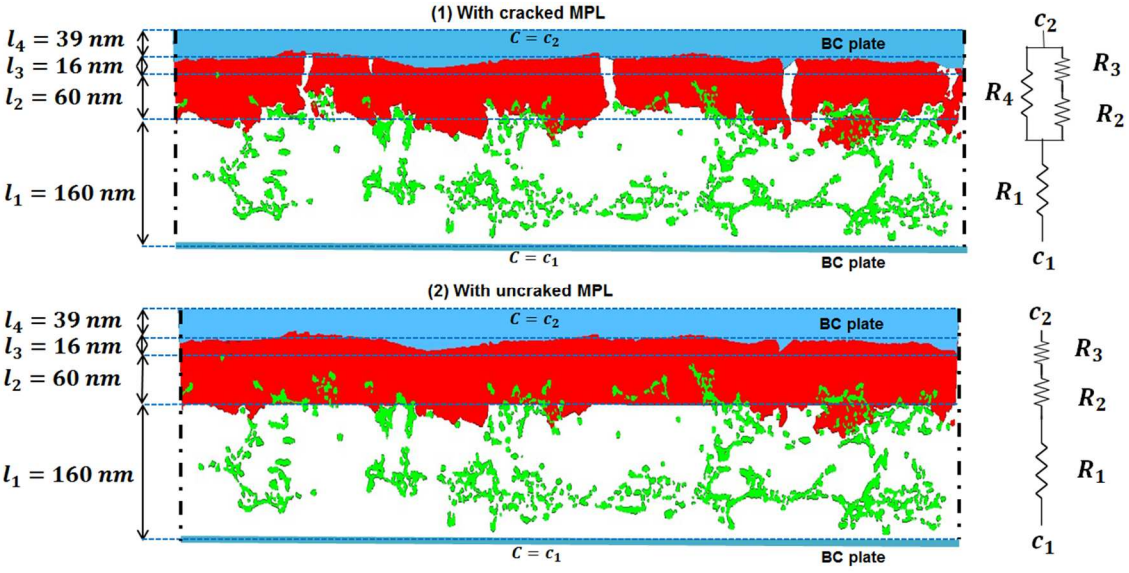

(b)

Fig. 8. a) Illustration of multiscale approach combining FIB-SEM (MPL matrix) and X-ray tomography images (GDM-MPL assembly) . The MPL 3D cracks network and the penetration of MPL (in red) in GDM (in green) are visible in the X-ray tomography images. b) Sketch of the various layers and equivalent resistance model. Expressions of the various resistances are given in Table 3.

In Fig.8, ℓ_1 is the thickness of the GDM region free of MPL: ℓ_1 is the vertical distance between first fiber (bottom) and average position of MPL bottom surface. The thickness of the GDM-MPL overlap region is denoted by ℓ_2: ℓ_2 is the vertical distance between the most advanced fiber and the average position of MPL bottom surface. The thickness of the MPL region free of fibers is ℓ_3: ℓ_3 is the vertical distance between the most advanced fiber and the average position of MPL top surface. A horizontal reference plane is defined at some distance from the MPL top surface to facilitate the implementation of the top boundary condition. The thickness of this additional layer is ℓ_4: ℓ_4 is the average vertical distance between the MPL top surface average position and this plane. To compute the assembly through-plane diffusion coefficient, the top BC ($C = c_2$) is applied over this top plane surface. The region in blue is a region where a large value of the diffusion coefficient (1 m^2/s, thus 10^5 greater than the diffusion coefficient in the pores) is imposed so that the diffusion transport resistance of this region is negligible. The bottom boundary condition ($C = c_1$) is imposed over the plane adjacent to the first fiber voxel in the vertical direction in the image.

As indicated in Table 2, the MPL reduces the porosity of the assembly by 8% to 10% depending on the presence of cracks or not compared to the GDM alone. The MPL thickness is about 76 µm in average, which agrees with the apparent MPL thickness of SGL 22BB characterized in [10]. The thickness of the GDM alone is about 220 µm, but there is an important overlap between the MPL and the GDM.

Table 2. GDM and GDM/MPL assembly through plane diffusion properties**.**

	GDM without MPL	GDL with cracked MPL	GDL with crack free MPL
Thickness ℓ (µm)	220	236	236
Porosity	0.88	0.81	0.8
Through plane effective relative diffusion coefficient $\frac{1}{\tau}$	0.8	0.66	0.6
Through plane diffusive resistance $R/R_{GDM-woMPL}$ ($R = \frac{\ell\tau}{\varepsilon D_{bulk}}$)	1	1.4	1.6

4.2.1 GDM through plane effective diffusion coefficient

A digital 3D-image of the GDM alone is obtained from the image of the GDM-MPL assembly by changing the MPL voxels into gas voxels. Then, the through plane effective diffusion

coefficient of the GDM alone is computed numerically solving the diffusion equation in the pore space using the same method as for the MPL effective diffusion tensor computation. Only the through plane component of the tensor is considered in what follows. This yields a relative diffusion coefficient $\frac{D_{effxx-GDM}}{D_{bulk}} = \frac{1}{\tau} \approx 0.8$. This value is in good agreement with the literature for the porosity ($\varepsilon = 0.88$) of the considered GDM. For example, a semi-analytical model based on the fiber organization was proposed in [50]. This model reads,

$$\frac{D_{eff}}{D_{bulk}} = \frac{1}{\tau} = \frac{1}{6}\left(\frac{4.7-1.7\varepsilon}{2.7-1.7\varepsilon} + \frac{9}{6.4-3.4\varepsilon}\right) \quad (16)$$

Applying Eq. (16) yields $\frac{1}{\tau} = 0.88$, which is, however, a bit larger than the value obtained from our simulations. As discussed in [50], another analytical model commonly used for fibrous medium reads,

$$\frac{D_{eff}}{D_{bulk}} = \frac{1}{\tau} = \left(\frac{\varepsilon-\varepsilon_p}{1-\varepsilon_p}\right)^{\zeta} \quad (17)$$

where ζ and ε_p are two parameters fitted from experiments. According to [50], $\varepsilon_p = 0.11$, $\zeta = 0.875$ for application to GDM. This leads to $\frac{1}{\tau} = 0.89$ that is again a bit greater than the value obtained from the simulations. This difference with the analytical model prediction is discussed in [27], where it is shown that the analytical or semi-analytical models overestimate the relative effective diffusion coefficient compared to the experiments. This is explained by the effect of the binder in the fibrous medium. The results presented in [50] can be described using a Bruggeman like relationship with an exponent -3, that is $\tau = \varepsilon^{-3}$, which for $\varepsilon = 0.88$ gives $\frac{1}{\tau} = 0.68$, lower than our value of 0.8. In this regard, it should be noticed that the GDMs considered in [50] are not from SIGRACET. They might contain more binder. Also, the GDL is compressed in [50], which is not the case of our GDL. This important point is further discussed in Section 5. Finally, as indicated in Table 2, the value of 0.8 from our simulations is in good agreement with the LBM simulations on reconstructed GDMs presented in [51], where a Bruggeman like relationship with an exponent 1.61 was found to represent the data obtained from the numerical simulations, i.e. $\tau = \varepsilon^{-1.61}$. For our data, a best fit leads to a slightly greater exponent, $\tau = \varepsilon^{-1.74}$.

4.2.2 GDM-MPL assembly through plane effective diffusion coefficient

In order to evaluate the impact of cracks in the MPL, two cases are considered: with and without cracks. To obtain a GDM-MPL assembly without cracks, the crack voxels are converted into MPL voxel according to the following procedure. Two planes are determined

by computing the average position of the more advanced (least advanced respectively) MPL voxels in the through plane direction in the image. These planes are illustrated in Fig. 8b and correspond to the horizontal planes separated by thickness $\ell_2 + \ell_3$. As illustrated in Fig.8b, all crack voxels located between these two planes are converted into MPL voxel to obtain the GDM-MPL assembly without cracks. Results of simulations are reported in Table 2. The calculation of the through plane effective diffusion coefficient of the GDL with MPL in Table 2 first shows the impact of the MPL. The effective diffusion coefficient is reduced by a factor 0.82 with the MPL with cracks and 0.75 with the crack free MPL compared to the value for the GDM alone. A somewhat similar significant reduction in the effective diffusion coefficient was reported in [38] from simulations over reconstructed GDM and MPL with a decrease of 40 % in the effective diffusion coefficient. As discussed in [39], the decrease in the effective diffusion coefficient compared to the GDM alone depends on the ratio between the MPL effective diffusion coefficient and that for the GDM as well as the size of the MPL-GDM overlapping region. Since the thickness of the GDM-MPL assembly is different from the thickness of the GDM alone, it is more insightful to discuss the results in term of overall diffusion resistance [27]. The diffusion flux through a layer of thickness ℓ is expressed as,

$$J = \mathcal{E} D_{eff} \frac{\Delta c}{\ell} = \mathcal{E} D_{bulk} \frac{1}{\tau} \frac{\Delta c}{\ell} = \frac{\Delta c}{R} \tag{18}$$

Where Δc is the concentration difference across the layer. Eq. (18) defines the layer diffusion resistance as $R = \frac{\ell \tau}{\mathcal{E} D_{bulk}}$. Using the data in Table 2, the MPL-GDM assembly diffusion resistance is 60 % larger in the presence of cracks and 80 % in the absence of cracks compared to the GDM alone. The crack free GDM-MPL diffusion resistance is therefore about 10% larger than for the GDM-MPL assembly with cracks. This is a clear indication that the cracks facilitate the oxygen access to the catalyst layer (when they are free of liquid water).

Table 3. Expression of diffusion resistances used in the resistance models sketched in Fig. 8.

	Cracked MPL	Uncracked MPL
R_1	$\frac{\ell_1 \tau_{GDM}}{\mathcal{E}_{GDM} D_{bulk}}$	$\frac{\ell_1 \tau_{GDM}}{\mathcal{E}_{GDM} D_{bulk}}$
R_2	$\frac{\ell_2 \tau_{overlap}}{(1-\mathcal{E}_c)\mathcal{E}_{overlap} D_{bulk}}$	$\frac{\ell_2 \tau_{overlap}}{\mathcal{E}_{overlap} D_{bulk}}$
R_3	$\frac{\ell_3 \tau_{MPL}}{(1-\mathcal{E}_c)\mathcal{E}_{MPL} D_{bulk}}$	$\frac{\ell_3 \tau_{MPL}}{\mathcal{E}_{MPL} D_{bulk}}$
R_4	$\frac{(\ell_2 + \ell_3)\tau_{MPL}}{\mathcal{E}_c D_{bulk}}$	-

An interesting question is the impact of the overlapping region between the GDM and the MPL [39]. Let-us assume no overlap. Then from the definition of the diffusion resistance, the diffusion resistance of the assembly is simply the sum of the MPL and GDM resistances,

$$\frac{(\ell_{GDM}+\ell_{MPL})\tau_{GDM-MPL}}{\varepsilon_{GDM-MPL}} = \frac{\ell_{GDM}\tau_{GDM}}{\varepsilon_{GDM}} + \frac{\ell_{MPL}\tau_{MPL}}{\varepsilon_{MPL}} \tag{19}$$

where $\ell_{GDM} = \ell_1 + \ell_2$ and $\ell_{MPL} = \ell_2 + \ell_3$. Using the data from Tables 1 and 2 and the thickness values indicated in Fig.8, this gives $1./\tau_{GDM-MPL}$= 0.64 in the case of an uncracked MPL, which is greater than the computed value of 0.6 (Table 2, uncracked MPL). The total diffusive resistance of the assembly in the absence of overlap is greater than the resistance with overlap ($\frac{R_{GDM-MPL-no-overlap}}{R_{GDM}}$ = 1.76 against 1.6 with the overlap without cracks in the MPL, Table 2), mainly due to the greater thickness of the assembly in the absence of overlap.

Referring to Fig. 8b, the consideration of the overlap zone in the resistance model leads to the following relationship,

$$\frac{(\ell_1+\ell_2+\ell_3)\tau_{GDM-MPL}}{\varepsilon_{GDM-MPL}} = \frac{\ell_1\tau_{GDM}}{\varepsilon_{GDM}} + \frac{\ell_2\tau_{overlap}}{\varepsilon_{overlap}} + \frac{\ell_3\tau_{MPL}}{\varepsilon_{MPL}} \tag{20}$$

where $\tau_{overlap}$ is the tortuosity of the overlap zone. The latter can be estimated from the relationship,

$$\tau_{overlap} = \frac{D_{bulk}}{D_{eff-overlap}} = \frac{D_{bulk}}{D_{eff-MPL}} \frac{D_{eff-MPL}}{D_{eff-overlap}} = \tau_{MPL}\tau_{GDM} \tag{21}$$

whereas the porosity in the overlap region is given by $\varepsilon_{overlap} = \varepsilon_{GDM}\varepsilon_{MPL}$. Using the latter relationship and Eq.(21) and applying Eq.(20) leads to $1/\tau_{GDM-MPL}$ = 0.53. This is smaller than the computed value (0.6 in Table 2 for the case of the crack free MPL) but clearly illustrates the impact of the overlap on the diffusion process [52] from the comparison with the value 0.64 in the absence of overlap.

In the case of the MPL with cracks the relative through plane effective coefficient is larger as shown in Table 2. Considering the cracks in the resistance model is not difficult as sketched in Fig.8b. This leads to the relationship,

$$\frac{(\ell_1+\ell_2+\ell_3)\tau_{GDM-MPL}}{\varepsilon_{GDM-MPL}} = \frac{\ell_1\tau_{GDM}}{\varepsilon_{GDM}} + \frac{1}{\frac{\varepsilon_c}{(\ell_2+\ell_3)}+(1-\varepsilon_c)\left(\frac{\ell_2\tau_{overlap}}{\varepsilon_{overlap}}+\frac{\ell_3\tau_{MPL}}{\varepsilon_{MPL}}\right)^{-1}} \tag{22}$$

where ε_c represents the crack volume fraction in the MPL. From image analysis, $\varepsilon_c \approx 16\%$. Applying Eq.(22) yields $\tau_{GDM-MPL}$ = 0.67, which is in excellent agreement with the numerical simulation computed value 0.66 reported in Table 2.

5. Impact of GDM compression

The GDM-MPL assembly is compressed in a PEMFC whereas the 3D digital image of the GDM-MPL assembly obtained via XCT illustrated in Figs. 2 and 8 corresponds to an uncompressed assembly. The compression of the MPL can be expected to be negligible compared to the GDM. It has been shown that the compression has an impact on the GDL transport properties, e.g. [53], [54] and references therein. Thickness compression rates in the range [15% - 47%] are for example considered in [54]. In this regard, it would be certainly interesting to obtain images of the compressed GDM-MPL assembly via XCT, as for instance in [27] or [54], and repeat the numerical simulations. However, since we do not have such images, insights on the impact of the compression can be gained by adapting Eq. (22). Considering that the MPL is not affected by the compression, the compression impacts the GDM thickness, porosity and tortuosity outside the overlap region where the GDM properties are assumed not affected by the compression. Following [55], the porosity of the GDM can be estimated from the relationship $\varepsilon_{GDL} = \frac{\varepsilon_0 - \alpha}{1-\alpha}$, where ε_0 is the porosity of the uncompressed GDM and α is the GDM thickness compression rate defined as $\alpha = \frac{\ell_0 - \ell}{\ell_0}$, where ℓ_0 is the thickness of the uncompressed medium and ℓ is that of the compressed medium. As discussed in Section 4.2.1, the GDM tortuosity can be described by a power law, namely $\tau_{GDL} = \varepsilon_{GDL}^{-1.74}$. Accordingly, Eq. (22) can be expressed as

$$\frac{(\ell_1(1-\alpha)+\ell_2+\ell_3)\tau_{GDM-MPL}}{\varepsilon_{GDM-MPL}} = \ell_1(1-\alpha)\left(\frac{\varepsilon_0-\alpha}{1-\alpha}\right)^{-2.74} + \frac{1}{\frac{\varepsilon_c}{(\ell_2+\ell_3)}+(1-\varepsilon_c)\left(\frac{\ell_2\tau_{overlap}}{\varepsilon_{overlap}}+\frac{\ell_3\tau_{MPL}}{\varepsilon_{MPL}}\right)^{-1}} \quad (23)$$

where $\varepsilon_{GDM-MPL} = \frac{\ell_1(1-\alpha)\left(\frac{\varepsilon_0-\alpha}{1-\alpha}\right)+\ell_2\varepsilon_{overlap}+\ell_3\varepsilon_{MPL}}{(\ell_1+\ell_2+\ell_3)}$.

As illustrated in Fig.9, the equivalent resistance model with compression shows that the impact of cracks on the assembly through plane diffusion coefficient compared to the case without cracks is similar at different compression ratio, a little bit more important at high compression. For a typical compression rate of 20%, the effective diffusion coefficient decreases by about 10%. Based on the results shown in Fig.9, it can be concluded that the impact of the compression is comparable in magnitude to the impact of the cracks

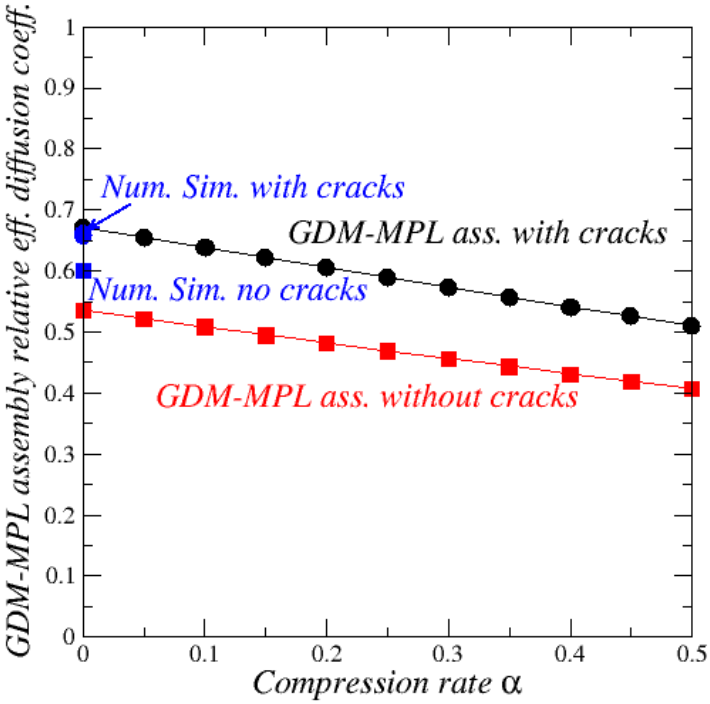

Fig. 9. GDM-MPL assembly through plane effective diffusion coefficient for different compression rates from equivalent resistance model (Eq.(23)).

6. Conclusion

The calculated effective diffusivity tensor from the MPL microstructure digital image data is diagonal, and almost isotropic for the length scales considered in the present study (minimum cube side of 250 nm).

A multiscale approach was developed to study the gas diffusion properties of the GDM-MPL assembly from numerical simulations on 3D -digital images obtained via FIB-SEM (MPL) and X-ray computed tomography (GDM, GDM-MPL assembly). The MPL matrix effective diffusion tensor was characterized and shown to be slightly anisotropic. The commonly used assumption of isotropy is therefore quite reasonable for the MPL sample size considered in the present study.

Knudsen diffusion is important in the MPL. It was shown that the effective diffusion coefficients (diagonal terms of the tensor) decrease by 40% compared to the computation considering the Fick diffusion only.

The simulation procedure was compared against experimental data confirming, as suggested in [48], that Bruggeman model with the exponent 0.5 overestimates the effective diffusion coefficient.

Computation of the through plane effective diffusion coefficient of the GDM-MPL assembly shows that the MPL has a quite significant impact on the GDM-MPL diffusion property

compared to the GDM alone. Consistently with previous works, the MPL-GDM overlap region has a quite noticeable impact on the diffusion resistance of the assembly. Somewhat surprisingly, MPL cracks have a relatively weak impact on the assembly diffusive resistance, with a reduction by about 10%.

An equivalent resistance model was used to characterize the GDM-MPL assembly through plane diffusion coefficient. This model was shown to be consistent with the numerical simulations. This model was used to explore the impact of the GDM compression on the diffusion property of the GDM-MPL assembly and it was found that the impact of the compression is on the same order of magnitude as the impact of the cracks in the MPL.

CRediT authorship contribution statement

Mohamed Ahmed-Maloum: Numerical simulations, modelling, Writing – original draft. Editing**. Thomas David:** FIB-SEM, image processing. **Laure Guetaz**: FIB-SEM supervision, Editing. **Paul Duru**: X-Ray tomography, **Joel Pauchet**: Conceptualization, Editing. **Michel Quintard**: Conceptualization, Modelling, Numerical simulation Supervision, Editing. **Marc Prat:** Conceptualization, Modelling, Writing – review & editing.

Declaration of Competing Interest

The authors declare that they have no known competing financial interests or personal relationships that could have appeared to influence the work reported in this paper.

Acknowledgements: This project has received funding from the Fuel Cells and Hydrogen 2 Joint Undertaking (now Clean Hydrogen Partnership) under Grant Agreement No 875025. This Joint Undertaking receives support from the European Union's Horizon 2020 Research and Innovation program, Hydrogen Europe and Hydrogen Europe Research.

References

1. M. Eikerling, A. A. Kornyshev, and A. R. Kucernak, "Water in polymer electrolyte fuel cells: Friend or foe?," Physics Today, vol. 59, pp. 38–44, Oct. 2006.
2. H. Liu, M.G. George, R. Zeis, M. Messerschmidt, J. Scholta, A. Bazylak, The impacts of microporous layer degradation on liquid water distributions in polymer electrolyte membrane fuel cells using synchrotron imaging, ECS Trans 80 (8) (2017) 155–164,
3. N. Holmström, J. Ihonen, A. Lundblad, G. Lindbergh, The influence of the gas diffusion layer on water management in polymer electrolyte fuel cells, Fuel Cell. 7 (4) (2007) 306–313.

4. Z. Qi, A. Kaufman, Improvement of water management by a microporous sublayer for PEM fuel cells, J. Power Sources 109 (1) (2002) 38–46,
5. H.K. Atiyeh, E. Halliop, J. Pharoah, K. Karan, A. Phoenix, B. Peppley, Experimental investigation of the role of a microporous layer on the water transport and performance of a PEM fuel cell, J. Power Sources 170 (1) (2007) 111–121.
6. J. Chen, T. Matsuura, M. Hori, Novel gas diffusion layer with water management function for PEMFC, J. Power Sources 131 (1–2) (2004) 155–161.
7. R. Lin, L. Chen, T. Zheng, S. Tang, X. Yu, M. Dong, Z. Hao, Interfacial water management of gradient microporous layer for self-humidifying proton exchange membrane fuel cells, Int. J. Heat Mass Tran. 175 (2021) 121340,
8. J.H. Nam, K.-J. Lee, G.-S. Hwang, C.-J. Kim, M. Kaviany, Microporous layer for water morphology control in PEMFC, Int. J. Heat Mass Tran. 52 (11–12) (2009) 2779–2791,
9. J.H. Nam, M. Kaviany, Effective diffusivity and water-saturation distribution in single- and two-layer PEMFC diffusion medium, Int. J. Heat Mass Tran. 46 (24) (2003) 4595–4611,
10. Y.-C. Chen, C. Karageorgiou, J. Eller, T. J. Schmidt, F. N. Büchi, Determination of the porosity and its heterogeneity of fuel cell microporous layers by X-ray tomographic microscopy. Journal of Power Sources 539 (2022) 231612
11. B. Straubhaar, J. Pauchet, M Prat, Pore network modelling of condensation in gas diffusion layers of proton exchange membrane fuel cells, International Journal of Heat and Mass Transfer 102, 891-901 (2016)
12. P.Carrère, M.Prat, Liquid water in cathode Gas Diffusion Layers of PEM fuel cells: identification of various pore filling regimes from pore network simulations, International Journal of Heat and Mass Transfer 129, 1043–1056 (2019)
13. L.Ceballos, M.Prat, Invasion percolation with multiple inlet injections and the water management problem in Proton Exchange Membrane Fuel Cells, J. of Power Sources 195, pp. 825–828(2010)
14. L. Ceballos, M. Prat, and P. Duru, Slow invasion of a non-wetting fluid from multiple inlet sources in a thin porous layer. Phys. Rev. E 84, 056311 (2011)
15. Z. Lu, M.M. Daino, C. Rath, S.G. Kandlikar, Water management studies in PEM fuel cells, Part III: dynamic breakthrough and intermittent drainage characteristics from GDLs with and without MPLs, Int. J. Hydrogen Energy 35 (9) (2010)4222–4233
16. J.T. Gostick, M.A. Ioannidis, M.W. Fowler, M.D. Pritzker, On the role of the microporous layer in PEMFC operation, Electrochem. Commun. 11 (3) (2009) 576–579,
17. X. Wang, T.V. Nguyen, Modeling the effects of the cathode micro-porous layer on the performance of a PEM fuel cell, ECS Trans 16 (2) (2019) 3–12,
18. A.Z. Weber, J. Newman, Effects of microporous layers in polymer electrolyte fuel cells. J. Electrochem. Soc. 152 (2005) A677.
19. M. Wang, S. Medina, J.R. Pfeilsticker, S. Pylypenko, M. Ulsh, S.A. Mauger, Impact of microporous layer roughness on gas-diffusion-electrode-based polymer electrolyte membrane fuel cell performance, ACS Appl. Energy Mater. 2 (11) (2019) 7757–7761
20. J. Shi, Z. Zhan, D. Zhang, Y. Yu, X. Yang, L. He, M. Pan, Effects of cracks on the mass transfer of polymer electrolyte membrane fuel cell with high performance membrane

electrode assembly, J. Wuhan Univ. Technol.-Materials Sci. Ed. 36 (3) (2021) 318–330,
21. Q.Chen, Z. Niu, H. Li, K. Jiao, Y. Wang Recent progress of gas diffusion layer in proton exchange membrane fuel cell: Two-phase flow and material properties. i nternational journal of hydrogen energy 46 (2 0 2 1) 8 6 4 0-8 6 7 1
22. E.A. Wargo, V.P. Schulz, A. Cesen, S.R. Kalidindi, E.C. Kumbur, Resolving macro- and micro-porous layer interaction in polymer electrolyte fuel cells using focused ion beam and X-ray computed tomography, Electrochimica Acta 87 (2013) 201– 212
23. D. Wildenschild, X-ray imaging and analysis techniques for quantifying pore-scale structure and processes in subsurface porous medium systems, Adv Water Resour, 51 (2013), pp. 217-246
24. C. Redenbach, K. Schladitz, M. Klingele, M. Godehardt, Reconstructing porous structures from FIB-SEM image data: Optimizing sampling scheme and image processing, Ultramicroscopy Volume 226, July 2021, 113291
25. H. Ostadi, P. Rama, Y. Liu, R. Chen, X.X. Zhang, K. Jiang, 3D reconstruction of a gas diffusion layer and a microporous layer, Journal of Membrane Science 351 (2010) 69–74
26. X.Zhang, Y Gao, H Ostadi, K Jiang, R Chen, Modelling water intrusion and oxygen diffusion in a reconstructed microporous layer of PEM fuel cells. International Journal of Hydrogen Energy, 39, (30), 2014, 17222-17230.
27. G. Inoue, K. Yokoyama, J. Ooyama, T. Terao, T. Tokunaga, N. Kubo, M. Kawase, Theoretical examination of effective oxygen diffusion coefficient and electrical conductivity of polymer electrolyte fuel cell porous components. Journal of Power Sources 327 (2016), pp. 610–621.
28. M. Andisheh-Tadbir, F. P. Orfino, E. Kjeang, Three-dimensional phase segregation of micro-porous layers for fuel cells by nano-scale X-ray computed tomography. Journal of Power Sources 310 (2016) 61-69.
29. S.Berg, D. Kutra, T. Kroeger, C. N. Straehle, B. X. Kausler, C. Haubold, M. Schiegg, J. Ales, T. Beier, M. Rudy, K. Eren, J. I Cervantes, B. Xu, F. Beuttenmueller, A. Wolny, C. Zhang, U. Koethe, F. A. Hamprecht, A. Kreshuk, ilastik: interactive machine learning for (bio)image analysis, Nature Methods, 16, 1226–1232 (2019).
30. S.S. Alrwashdeh, I. Manke, H. Marko, M. Klages, M. Go, In operando quantification of three- dimensional water distribution in nanoporous carbon-based layers in polymer electrolyte membrane fuel cells. *ACS Nano* 2017, 11, 6, 5944–5949
31. R. Banerjee, J. Hinebaugh, H. Liu, R. Yip, N. Ge, A. Bazylak, Heterogeneous porosity distributions of polymer electrolyte membrane fuel cell gas diffusion layer materials with rib-channel compression, Int. J. Hydrogen Energy 41 (33) (2016) 14885–14896,
32. D. Muirhead, R. Banerjee, J. Lee, M.G. George, N. Ge, H. Liu, S. Chevalier, J. Hinebaugh, K. Han, A. Bazylak, Simultaneous characterization of oxygen transport resistance and spatially resolved liquid water saturation at high-current density of polymer electrolyte membrane fuel cells with varied cathode relative humidity, Int. J. Hydrogen Energy 42 (49) (2017) 29472–29483,

33. A.Kai, C. Wong, R. Banerjee, A. Bazylak, Tuning MPL Intrusion to Increase Oxygen Transport in Dry and Partially Saturated Polymer Electrolyte Membrane Fuel Cell Gas Diffusion Layers, 2019 J. Electrochem. Soc. 166 F3009
34. Gostick J, Khan ZA, Tranter TG, Kok MDR, Agnaou M, Sadeghi MA, Jervis R. PoreSpy: A Python Toolkit for Quantitative Analysis of Porous Media Images. Journal of Open Source Software, 2019.
35. F.E. Hizir, S.O. Ural, E.C. Kumbur, M.M. Mench, Characterization of interfacial morphology in polymer electrolyte fuel cells: Micro-porous layer and catalyst layer surfaces. J. Power Sources 195 (2010) 3463-3471
36. T. Sasabe, P. Deevanhxay, S.Tsushima, S. Hirai Soft X-ray visualization of the liquid water transport within the cracks of micro porous layer in PEMFC Electrochemistry Communications Volume 13, Issue 6, June 2011, Pages 638-641
37. X. Shi, D. Jiao, Z. Bao, K. Jiao, W. Chen, Z. Liu, Liquid transport in gas diffusion layer of proton exchange membrane fuel cells: Effects of microporous layer cracks, International Journal of Hydrogen Energy 47 (2022) 6247 – 6258.
38. M. Knudsen, Die Gesetze der Molekularströmung und der inneren Reibungsströmung der Gase durch Röhren, Ann. Phys. (Leipzig), 28 (1909), pp. 75-130
39. J. Becker, C. Wieser, S. Fell, K. Steiner. A multi-scale approach to material modeling of fuel cell diffusion media. International Journal of Heat and Mass Transfer 54.7 (2011), pp. 1360–1368.
40. W.G. Pollard, R.D. Present. On gaseous self-diffusion in long capillary tubes. Phys. Rev. 73, 762–774 (1948).
41. V.Novák, F.Štěpánek, P.Kočí, M.Marek, M.Kubíček, Evaluation of local pore sizes and transport properties in porous catalysts, Chemical Engineering Science Volume 65, Issue 7, 1 April 2010, Pages 2352-2360
42. R. Krishna, J. M. van Baten. Investigating the validity of the Bosanquet formula for estimation of diffusivities in mesopores. Chemical Engineering Science 69.1 (2012), pp. 684–688.
43. S.Whitaker. The Method of Volume Averaging. Springer Science & Business Media. 2013
44. M. Kfoury, R. Ababou, B. Noetinger, M. Quintard. Upscaling Fractured Heterogeneous Media: Permeability and Mass Exchange Coefficient. Journal of Applied Mechanics 73(1): 41-46 (2006)
45. L. J. Durlofsky, Upscaling of Geocellular Models for Reservoir Flow Simulation: A Review of Recent Progress, Paper presented at 7th International Forum on Reservoir Simulation, Buhl/Baden-Baden, Germany, June 23-27, 2003
46. R. Guibert, P.Horgue, G.Debenest, M.Quintard, A Comparison of Various Methods for the Numerical Evaluation of Porous Media Permeability Tensors from Pore-Scale Geometry. Mathematical geosciences 48, 2016, pp. 329–347.
47. A.Bamberger (1977). Approximation des coefficients d'opérateurs elliptiques stables pour la G-convergence. Technical report
48. B. Tjaden, S. J. Cooper, D. J. L. Brett, D. Kramer, P. R Shearing, On the origin and application of the Bruggeman correlation for analysing transport phenomena in electrochemical systems, Current Opinion in Chemical Engineering Volume 12, May 2016, Pages 44-51.

49. Y Guo, X He, W Huang, M Wang, Microstructure Effects on Effective Gas Diffusion Coefficient of Nanoporous Materials. Transport in Porous Media 126 (2019), pp. 431–453.
50. J. Jankovic, S.Zhang, A. Putz, M. S. Saha, D. Susac. Multiscale imaging and transport modeling for fuel cell electrodes. Journal of Materials Research 34 (4), 2019 , 579 – 591.
51. X. Huang, W. Zhou, D. Deng. Effective Diffusion in Fibrous Porous Media: A Comparison Study between Lattice Boltzmann and Pore Network Modeling Methods. Materials 14.4 (2021). 1996-1944.
52. X Zhang, J Yang, X Ma, W Zhuge, S Shuai. Modelling and analysis on effects of penetration of microporous layer into gas diffusion layer in PEM fuel cells: Focusing on mass transport. Energy 124103 (2022), pp. 610–621.
53. T.Nitta, O.Hottinen, M. Himanea, M. Mikkola, Inhomogeneous compression of PEMFC gas diffusion layer: Part I. Experimental, Journal of Power Sources, 171 (1), 2007, 26–36.
54. V. Zenyuk, D.Y. Parkinson, G. Hwang, A.Z. Weber, Probing water distribution in compressed fuel-cell gas-diffusion layers using X-ray computed tomography, Electrochem. Commun. 53 (2015) 24–28.
55. P.H. Chi, S.H. Chan, F.B. Weng, A. Su, P.C. Sui, N. Djilali. On the effects of non-uniform property distribution due to compression in the gas diffusion layer of a PEMFC. Int. J. Hydrogen Energy 35:2936-2948 (2010).